Journal of Remote Sensing
A SCIENCE PARTNER JOURNAL

RESEARCH ARTICLE

Precision Mapping of Coastal Wetlands: An Integrated Remote Sensing Approach Using Unoccupied Aerial Systems Light Detection and Ranging and Multispectral Data

Narcisa Gabriela Pricope[1*], Joanne Nancie Halls[2], Elijah Garrett Dalton[3], Asami Minei[2], Cuixian Chen[4], and Yishi Wang[4]

[1]Department of Geosciences, Mississippi State University, Starkville, MS 39579, USA. [2]Department of Earth and Ocean Sciences, University of North Carolina Wilmington, Wilmington, NC 28409, USA. [3]Spatial Informatics Group LLC, Pleasanton, CA 94566, USA. [4]Department of Mathematics and Statistics, University of North Carolina Wilmington, Wilmington, NC 28409, USA.

*Address correspondence to: npricope@research.msstate.edu

Citation: Pricope NG, Halls JN, Dalton EG, Minei A, Chen C, Wang Y. Precision Mapping of Coastal Wetlands: An Integrated Remote Sensing Approach Using Unoccupied Aerial Systems Light Detection and Ranging and Multispectral Data. *J. Remote Sens.* 2024;4:Article 0169. https://doi.org/10.34133/remotesensing.0169

Submitted 14 December 2023
Accepted 4 June 2024
Published 4 July 2024

Coastal wetlands, crucial for global biodiversity and climate adaptation, provide essential ecosystem services such as carbon storage and flood protection. These vital areas are increasingly threatened by both natural and human-induced changes, prompting the need for advanced monitoring techniques. This study employs unmanned aerial systems (UASs) equipped with light detection and ranging (LiDAR) and multispectral sensors to survey diverse wetland types across 8 sites in North Carolina. Utilizing high-resolution elevation data and detailed vegetation analysis, coupled with sophisticated machine learning algorithms, we achieved differentiated and highly precise classifications of wetland types. Classification accuracies varied by type, with estuarine intertidal emergent wetlands showing the highest classification accuracies due to less complex vegetation structure and clearer spectral signatures, especially when collections account for tidal influence. In contrast, palustrine forested and scrub–shrub wetlands presented lower accuracies, often due to the denser, mixed, and more complex vegetation structure and variable inundation levels, which complicate spectral differentiation and ground returns from LiDAR sensors. Overall, our integrated UAS-derived LiDAR and multispectral approach not only enhances the accuracy of wetland mapping but also offers a scalable, efficient, and cost-effective method that substantially advances conservation efforts and informs policy-making for coastal resilience. By demonstrating the usefulness of small-scale aerial data collection in ecological mapping, this study highlights the transformative potential of merging advanced technologies in environmental monitoring, underscoring their critical role in sustaining natural habitats and aiding in climate change mitigation strategies.

Introduction

Coastal wetlands, situated at the interface between terrestrial and aquatic ecosystems, are either seasonally or permanently inundated [1]. These dynamic environments undergo constant transformations due to river erosion and deposition, vegetation growth, and human activities [2]. Recognized as one of the most productive ecosystems, coastal wetlands provide critical habitats for diverse plant and wildlife species [3,4]. Their significant capacity to sequester carbon categorizes them as crucial carbon sinks [4]. Notably, salt marshes within these wetlands can achieve biomass productivities as high as 3,000 g C/m^2/year, surpassing some agricultural outputs [5]. Beyond carbon sequestration, coastal wetlands buffer against storm runoff, enhance water quality, filter agricultural and industrial pollutants, recharge groundwater reserves, and bolster biodiversity [4]. They also offer aesthetic, spiritual, and recreational values [6] and are valued alongside tropical rainforests as economically pivotal ecosystems, estimated at US $10,000 per hectare [6,7].

Despite their ecological significance, coastal wetlands face mounting threats from natural and anthropogenic stressors, including dredging, eutrophication, habitat fragmentation, urban development, and rising sea levels [4,7]. Historically, between 25 and 50% of the world's coastal wetlands were repurposed for agriculture or aquaculture in the 20th century, with forecasts suggesting an additional loss of 20 to 45% due to sea level rise this century [7].

Mapping and monitoring coastal wetlands pose significant challenges due to their complex spatial scales and periodic flooding, which restricts accessibility and complicates traditional surveying methods [8]. In particular, forested coastal wetlands are difficult to map because of their dense or overlapping canopies [9] and the constant shift in tidal waters [10]. Initially, the US National Wetland Inventory (NWI) in the 1970s and 1980s marked a significant advancement by utilizing

satellite technology, albeit at coarse spatial resolutions with extensive temporal intervals [2]. However, these data are now outdated and fail to capture smaller, fragmented wetlands, particularly in areas like North Carolina where wetlands constitute 76.3% (3,100,703 acres) of the state's land [11].

In recent years, advancements in airborne and satellite remote sensing, coupled with the increasing use of unoccupied aircraft systems (UAS), have significantly improved the mapping of coastal wetlands [12]. UAS enable the capture of high-resolution imagery on demand, addressing the inefficiencies of historical wetland mapping methods. The advent of UAS has been spurred by technological advances in miniaturization and cost reduction, facilitating their use across various Earth science applications [10]. Remote sensing now frequently achieves hyperspatial resolutions of less than 1 m^2, enhancing the detail and accuracy of wetland classification and analysis [13].

The primary sensors employed in UAS-based analysis of coastal wetlands include multispectral and LiDAR (light detection and ranging) systems. Multispectral sensors are particularly effective for vegetation classification and soil moisture evaluation [14], while LiDAR sensors provide detailed elevation and vegetation structure data, essential for hydrological and ecological studies [15–19]. However, the accuracy of UAS-derived elevation data can vary, particularly in densely vegetated wetlands [20,21]. Despite these challenges, the integration of LiDAR and multispectral data has proven beneficial in refining wetland classifications and enhancing the precision of ecological models [22,23].

Given the complexity and vast scale of UAS-collected LiDAR and multispectral datasets, machine learning algorithms have become a practical solution for classifying wetlands through either supervised or unsupervised methods [17,24–26]. Among these, random forests (RF) is favored for its high accuracy, ability to handle varied data types, and straightforward interpretability [27–29]. The potential to fuse LiDAR and multispectral data in wetland classifications, assessing their comparative effectiveness, remains a crucial area of research and development, calling for further case studies [20,30].

This study aims to quantify the metrics derived from UAS-derived LiDAR point clouds and multispectral imagery across wetlands from palustrine to estuarine environments at 8 data collection sites. We evaluated these metrics' effectiveness in predicting the presence, extent, and types of wetlands. Utilizing LiDAR, we specifically aimed to address challenges in generating accurate surface models from imagery in sparsely vegetated areas [20,21]. We compared remotely sensed wetland delineations with traditional survey methods from the North Carolina Department of Transportation (NCDOT) and concurrent in situ ground reference point (GRP) data. Our research addresses 2 primary questions:

1. Can the integration of UAS-derived LiDAR topographic derivatives and canopy height data, along with multispectral imagery, accurately classify coastal wetlands by functional type across varying coastal environments from palustrine to estuarine?

2. What are the most critical variables for predicting the presence of functional coastal wetlands along a gradient from salt marshes to freshwater and forested wetlands?

Materials and Methods

Study area and data collection platforms

We collected UAS LiDAR and multispectral data, along with in situ reference data, at 7 sites across the Atlantic Coastal Plain. These sites represent a gradient of wetland types from palustrine to riverine to estuarine along the southeastern coast of North Carolina (Fig. 1 and Table 1). Surveys were conducted once per site between May 2020 and February 2021. However, Masonboro Island—experiencing the largest tidal range in our study—was surveyed twice, during both low and high tide conditions, resulting in a total of 8 field surveys across 7 sites. The data spanned 4 coastal counties—Brunswick, New Hanover, and Pender—which are among the fastest growing in terms of human population on the North Carolina coast.

The wetland classifications used in this study adhere to frameworks established at state, regional, and national levels [31], employing the Cowardin system, which was initially designed for inventorying U.S. wetlands and deep-water habitats, and later revised in 2013 [32]. While ecologically, deep-water habitats do not constitute wetlands, they are included in the classification as "permanently flooded lands lying below the deep-water boundary of wetlands" to ensure broader applicability. The Cowardin hierarchy is organized into 5 main systems: marine, estuarine, riverine, lacustrine, and palustrine, each further divided into subsystems, classes, dominance types, and modifiers (Table 1). In this research, we use the class level to categorize wetland types, treating areas permanently flooded within these systems, such as unconsolidated bottom or shore, as water bodies.

The palustrine system, significant in southeastern North Carolina, typically comprises inland wetlands situated between the tidal estuarine and the nontidal riverine and lacustrine systems. Despite traditionally being nontidal, these areas are becoming increasingly tidal as sea levels rise, underscoring their dynamic nature.

For the 8 surveys at the 7 sites, the field data collection equipment included a DJI Matrice 600 Pro equipped with a Quanergy LiDAR sensor, 2 Trimble RTK systems (an R8 for static collection and an R10 for GCP collection), and an eBee Plus RTK system fitted with a Parrot Sequoia multispectral camera (Fig. 2). Detailed descriptions of all equipment and survey methodologies are provided below.

UAS data collection and preprocessing for wetland mapping

For LiDAR data acquisition, we utilized the DJI Matrice 600 Pro (M600 Pro), a 6-rotor UAS with an A3 Pro flight controller

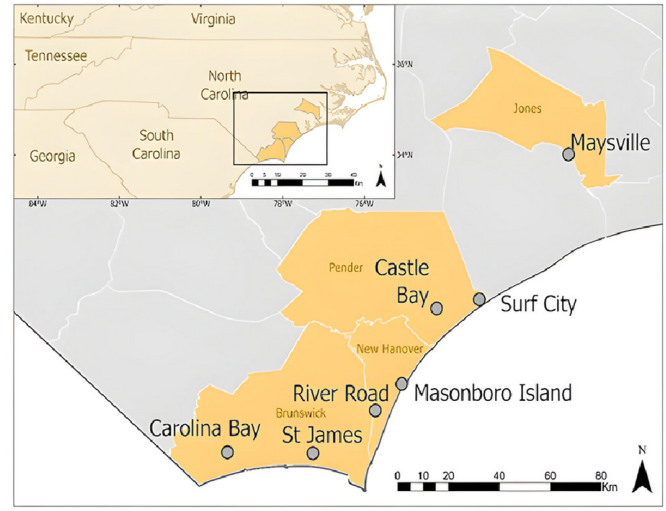

Fig. 1. Study area in southeastern NC showing the 8 collection locations across 4 coastal counties.

Table 1. Wetland types, NWI codes, and descriptions characteristic of the wetlands found in the study area

Wetland type	Wetland code	Description
Estuarine intertidal emergent	E2EM	The estuarine system consists of deep-water tidal habitats and adjacent tidal wetlands that are usually semi-enclosed by land but have open access to the open ocean. This system is characterized by the presence of intertidal and emergent vegetation. In southeastern North Carolina, the E2EM wetlands are dominated by the saltmarsh species *Spartina alterniflora* and along the higher marsh edges *Juncus roemerianus* is found.
Palustrine forest	PFO	The palustrine system includes inland, nontidal wetlands characterized by the presence of bottomland hardwood swamp forests, dominated by Cypress, sweet gum, and black gum. Additionally, there are pine flatlands, most notably the longleaf pine, that dominate this forested wetland.
Palustrine emergent	PEM	The palustrine system includes inland, nontidal wetlands characterized by the presence of emergent vegetation in bogs and freshwater marshes, and this is the least prevalent wetland type.
Palustrine scrub–shrub	PSS	The palustrine system includes inland, nontidal wetlands characterized by the presence of scrub–shrub, which is woody vegetation less than 20 ft tall. In southeastern North Carolina, the dominant PSS is pocosin wetlands where there is poor drainage and dense vegetation such as evergreen yaupon and thorny vines.

and Lightbridge 2 HD transmission, capable of reaching speeds up to 65 km/h. It was equipped with 6 TB48S batteries, enhancing its flight endurance. The UAS carried an 800-g Quanergy M8 LiDAR sensor alongside a Zenmuse X3 camera for in-flight video monitoring, crucial for ensuring operational safety. The Quanergy M8, an 8-laser scanner, boasts a 150-m range with 5-cm accuracy, and features a comprehensive 360-degree horizontal and 20-degree vertical field of view [9].

Parallelly, photogrammetric data were captured using a 1.3-kg eBee Plus RTK drone, integrated with a Parrot Sequoia multispectral sensor, characterized by its 116-cm wingspan and the ability to cover extensive areas with a 2.5-cm ground sampling distance (GSD) at 122-m altitude. The eBee Plus RTK's efficiency is underscored by its compatibility with FAA Part 107 regulations, permitting flight durations up to 59 min. The Sequoia sensor's configuration includes 4 multispectral bands (green, red, red edge, and near-infrared) and a low-resolution RGB camera, which are pivotal for detailed vegetation analysis.

The operational protocol involved meticulous flight mission planning, including the strategic placement of ground control points (GCPs) within 15 m of flight paths to enhance the spatial accuracy of the collected data. GCPs, recorded using Trimble RTK systems (R8 for static GPS data and R10 for GCP collection), underpin the georeferencing accuracy of the ensuing models. On the day of operation, 1 × 1 m GCP targets were deployed at predetermined locations, their positions accurately documented with ~2-cm precision.

LiDAR preprocessing entailed an intricate workflow: kinematic corrections using NovAtel Inertial Explorer, laser point positioning and GCP-corrected point cloud generation in ScanLook PC, followed by noise removal and vertical accuracy assessment with Global Mapper's LiDAR Quality Control tool and CloudCompare [18]. The processed LiDAR data facilitated the creation of comprehensive topographic models, including digital elevation models (DEMs) and digital surface models (DSMs), through ArcGIS Pro. These models served as foundational layers for generating topographic and vegetation indices crucial for wetland delineation.

Similarly, the photogrammetric data underwent postprocessed kinematic (PPK) correction in eMotion, followed by SfM-MVS processing in Pix4D Mapper Pro. This advanced processing technique enabled the reconstruction of 3-dimensional (3D) landscapes from 2D images, leveraging the spatial geometry captured from multiple vantage points [33–35]. The resulting georeferenced multispectral imagery, calibrated against the same GCPs used for LiDAR, yielded high-resolution reflectance rasters. These rasters were instrumental in computing vegetation and moisture indices [normalized difference vegetation index (NDVI), normalized difference red edge (NDRE), and normalized difference water index (NDWI)], providing a nuanced understanding of the wetland ecosystems under study (Table 2).

Field collection—Habitat reference points

Two Trimble RTK systems were employed to collect static data during UAS flights. These included GCPs for correcting UAS data and habitat GRPs for training image classification models. To train the models, half of the habitat GRPs were randomly selected, with the remainder used for accuracy assessment. To mitigate locational bias, GRP sample locations were generated using NWI data as a reference. We randomly generated an average of 15 points per wetland class (with 3 to 5 classes typically present at each site) and 50 points for nonwetland areas using the Spatially Balanced Points tool in ArcGIS Pro. Due to the diversity within nonwetland areas—including upland grass, developed land, and open water—more habitat points were collected in these areas compared to the wetland classes.

The randomly generated points were subsequently transferred to the Trimble R10 GNSS RTK GPS for field collection. On the day of the UAS flights, habitat GRPs were surveyed by navigating as close as possible to the generated points and collecting data

Fig. 2. Data collection platforms used in this study consisted of (A) DJI Matrice 600 Pro equipped with the Quanergy M8 LiDAR sensor, (B) Trimble RTK R8 used for static collections, (C) Trimble RTK R10 along with 1 × 1 m GCP targets, and (D) fixed wing eBee Plus RTK equipped with the Parrot Sequoia multispectral sensor.

using the Topo method while also recording the corresponding wetland class. As is common in wetland mapping, many planned points were physically inaccessible due to challenging topography, dense vegetation, or water inundation. These inaccessible points were documented during the fieldwork. Back in the laboratory, GRPs for wetland type and confidence level were determined using on-screen photointerpretation of 2020 National Agriculture Imagery Program (NAIP) imagery and data collected by our eBee-equipped multispectral camera. The 2020 true color NAIP imagery, available through the USDA's data gateway (https://datagateway.nrcs.usda.gov/GDGHome_DirectDownLoad.aspx), served as a valuable supplementary data source because it was approximately contemporary with our field surveys. Table 3 summarizes the general site characteristics, fieldwork dates, and the number of GCPs and GRPs collected for each site, either directly in the field or through visual interpretation of NAIP and high-resolution multispectral imagery.

RF modeling and analysis

After ensuring that all data were resampled to a uniform spatial resolution of 0.3 m and properly aligned within the area of interest (AOI) of each collection site, we utilized the h2o package in RStudio [36,37]. Once the raster stacks were prepared, we applied the K-fold cross-validation (CV) method to the RF algorithm in this study (Fig. 3). CV is a resampling technique favored for its ability to evaluate the overall performance and stability of predictive models while preventing overfitting [38]. In our analysis, RF classification was executed using a 5-fold CV algorithm, trained with field-collected and visually interpreted GRPs [39,40]. The selection of this algorithm was influenced by its favorable comparison with other machine learning algorithms, such as K-nearest neighbors (KNNs) and support vector machine (SVM) classifiers, in previous studies [41].

Initially, data for each site were randomly shuffled and divided into 5 equally sized folds. In the first run, we reserved the first fold as the testing set and used the remaining 4 folds for training a RF model. This model was then tested using the first fold to determine its classification accuracy. This procedure was repeated 4 additional times, cycling each fold as the testing set, which ultimately produced 5 RF models, each with a corresponding classification accuracy. The average and standard deviation of these 5 accuracies were calculated as key performance metrics.

Two critical parameters for the RF models included the number of decision trees (ntree), set to a default of 500, and the number of variables to consider at each split (mtry), which was equal to the number of input predictors. With 13 predictors in total, we chose 4 variables per split, and the seed for randomization was set at 1,122.

Post-processing activities involved generating prediction maps and calculating performance metrics. We computed 5 key model performance metrics: averaged overall accuracy, the

Table 2. Summary showing the predictors and response variables derived from the UAS-collected LiDAR and multispectral data

Raster layer	Variable	Data input	Definition
1	DSM	Digital surface model	Max height elevation in meters (including vegetation and artificial objects) [68]
2	DEM	Digital elevation model	Ground elevation in meters (vegetation and artificial objects removed) [68]
3	sDEM	Smoothed DEM	Ground elevation in meters, where microtopographic noise is removed [69]
4	hDEM	Hydro-condition DEM	Hydro-conditioning resolves topographic depressions before modeling flow paths [70]
5	Aspect	Aspect	Compass direction of the steepest downhill gradient
6	Slope	Slope	The rate of change of elevation per DEM cell
7	Curvature	Curvature	Combined curvature value from PlanCurv and ProfileCurv
8	PlanCurv	Plan curvature	The horizontal curvature of the slope (Curvature) [71]
9	ProfileCurv	Profile curvature	The vertical curvature of the slope (Curvature) [71]
10	NDVI	Normalized difference vegetation index $\frac{(NIR-RED)}{(NIR+RED)}$	Uses the contrast of vegetation between near-infrared and red light to calculate the relative biomass in an area [72]
11	NDWI	Normalized difference water index $\frac{(GREEN-NIR)}{(GREEN+NIR)}$	An index that is used to measure the water content in vegetation at the canopy level [73]
12	NDRE	Normalized difference red edge index $\frac{(NIR-REDEdge)}{(NIR+REDedge)}$	Measures the relative chlorophyll in plants due to reflecting light [74]
13	CHM	Canopy height model	Maps the height of the canopy layer as a continuous function [75]

standard deviation of accuracies, kappa coefficient, and class-level sensitivity and specificity. These metrics were derived from the accuracies of the 5-fold CV method and a confusion matrix. Additionally, we used standard variable importance plots to assess and rank the significance of various classification variables based on their impact on model accuracy when excluded. This approach allowed us to identify and quantify the most influential variables in classifying coastal wetland types.

To facilitate comparisons across sites and rank the most impactful variables, variable scores (ranging from 0.0 to 1.0) were converted to ranks (1 to 13), highlighting variables with scores above 0.7 as particularly significant.

The RF prediction model for each surveyed site was produced in raster format and visualized using ArcGIS Pro. Last, we conducted an assessment of overall model accuracy using all predictors across all 8 sites and a spatial assessment of GRP allocation correctness by functional wetland class compared to the final classification output [42].

Results and Discussion

Field data collection accuracy

A fundamental aspect of this project was establishing a reliable foundation for accurate LiDAR data collection using a UAS platform. To determine the optimal flight altitude and degree of overlap between flight lines, we conducted multiple tests over a densely forested 30-acre site. Previous studies have indicated that flying at lower altitudes increases the spatial resolution of the data, albeit at the cost of longer flight times necessary to cover the area [43]. However, altitude has been identified as a critical parameter in UAS LiDAR data collection [44], and other studies suggest that the percentage of flight line overlap may be more significant than altitude in certain contexts [45].

In our experiments, we tested 3 different flight altitudes (50, 60, and 65 m) and 3 percentages of overlap (10%, 25%, and 50%). The results indicated that the percentage of overlap had a more substantial impact on the point density of UAS LiDAR data than the altitude, albeit with specific nuances. For densely forested areas, a flight altitude of 65 m with a 25% overlap was found to produce the most reliable and dense point clouds. In contrast, less vegetated or bare areas yielded the highest point density with a flight combination of 50-m altitude and 25% overlap. Consequently, we adopted a standardized flight altitude of 60 m and an overlap of 25% for all our site surveys.

Table 4 details the accuracy data for each site, including the vertical accuracies [root mean square error in the z direction (RMSEz)] of the LiDAR point clouds relative to ground control and check points, as well as the horizontal (x, y) RMSE for the

Table 3. Field site characteristics, wetland type, date field work was conducted, size of the UAS survey (in acres), number of GCPs, and number of GRPs collected at each site.

Site name	General characteristics	Wetland type	Survey date	Size (acres)	Number of GCPs	Number of GRPs collected in field	Total number of GRPs
St James	Managed freshwater wetlands surrounded by residential development	PFO, PSS	5/12/2020	178.0	8	24	108
Castle Bay	Mixed managed wetlands and dense scrub/shrub	PFO, PEM, PSS	6/29/2020	164.2	7	34	172
River Rd	Palustrine forest and estuarine salt marsh	PFO, PEM	10/3/2020	54.34	11	29	137
Surf City	Estuarine salt marsh	E2EM, PFO, PSS	11/6/2020	78.28	15	18	157
Masonboro High Tide	Marine and estuarine barrier island	E2EM	12/7/2020	109.98	17	43	153
Masonboro Low Tide	Marine and estuarine barrier island	E2EM	12/11/2020	109.98	17	43	153
Maysville	Palustrine mixed forested wetlands	PFO	1/22/2021	43.80	9	27	81
Carolina Bay	Mixed forested wetlands with degraded wetlands	PFO	2/23/2021	59.4	13	15	34

collected multispectral imagery, all calculated in accordance with the American Society of Photogrammetry and Remote Sensing (ASPRS) guidelines for photogrammetry and LiDAR processing. All collected imagery and LiDAR data conformed to class A accuracy standards for photogrammetric work as stipulated by the ASPRS.

As anticipated, horizontal positioning demonstrated greater accuracy and precision compared to vertical measurements. The average horizontal dilution of precision (DOP) was below 2 cm, which is considered excellent, and the standard deviation among the sites was notably low, indicating minimal variability in accuracy across different locations. Interestingly, sites with a higher number of GRPs and GCPs, such as Surf City and Masonboro, did not exhibit significantly better horizontal or vertical accuracies.

Functional wetland type classification accuracy

We conducted a quantitative comparison of model performance metrics—including overall accuracies, standard deviations of overall accuracies, kappa coefficients (κ), sensitivities, and specificities—and the prediction maps generated using hyperspatial UAS LiDAR (Quanergy M8), UAS-collected multispectral data (Parrot Sequoia), and habitat GRPs. These evaluations primarily focused on the functional wetland types addressed in this study. It was hypothesized that elevation data and vertical vegetation metrics derived from UAS LiDAR datasets would enhance wetland classification compared to relying solely on stereophotogrammetry-based DSM measures, especially when combined with multispectral-derived indices [22,23,46–48].

The RF UAS classification model generally performed well across the 9 surveyed locations (Fig. 4). The estuarine site at Masonboro Island, characterized by an absence of dense forest canopy and where LiDAR data were collected at both low and high tides (but multispectral data only at low tide), demonstrated the highest overall classification accuracy (85.62% with κ of 0.782 at high tide and 82.24% with κ of 0.731 at low tide). The next highest accuracy was recorded at St. James, primarily a palustrine forested and scrub–shrub site, with an accuracy of 78.70% and a κ of 0.676. This performance is notable, especially given the tidal challenges associated with estuarine sites.

Conversely, the sites with the lowest classification accuracies faced more challenging conditions. Carolina Bay had the lowest accuracy at 70.59%, compounded by the smallest number of GRPs available for collection in the field and significant land cover changes relative to NWI data. Castle Bay, which includes dense forest and wetland environments as well as a golf course, recorded an accuracy of 66.46%. Both sites were hindered by difficult field conditions such as standing water, deep mud, inaccessible terrain, and private property, complicating the collection of training and validation points.

Moreover, the Carolina Bay site, which was also the smallest surveyed location, exhibited a large standard deviation and

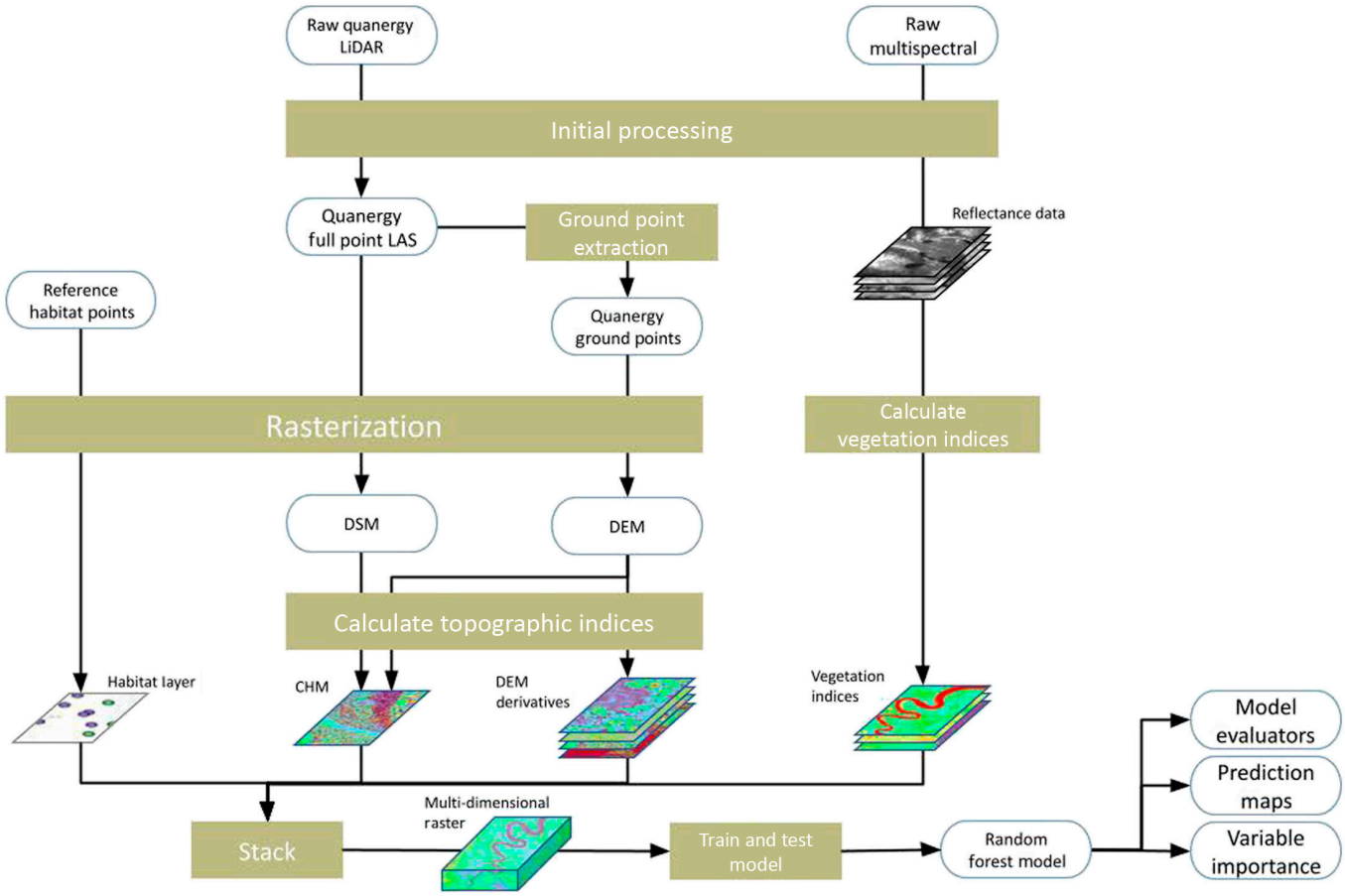

Fig. 3. Data processing and analysis workflow, where circular boxes represent input and output files, and olive boxes represent processing steps. The diagram shows the 13 predictor variables [CHM, DEM derivatives (9), and vegetation indices (3)] and reference habitat points (also known as GRPs, variable from site to site as indicated in Table 2) used in the final model.

Table 4. Site vertical accuracy (root mean square error) for both unconstrained and constrained UAS LiDAR point cloud horizontal accuracy for multispectral UAS imagery and RTK horizontal and vertical accuracies for the GCPs and GCPs

Site Name	LiDAR RMSEz (m) Unconstrained	LiDAR RMSEz (m) Constrained	Multispectral RMSE (m) *X*,*Y*	GCP horizontal precision (m)	GCP vertical precision (m)	GRP horizontal precision (m)	GRP vertical precision (m)
St James	0.187	0.34	0.024	0.008	0.013	0.012	0.02
Castle Bay	0.446	0.169	0.008	0.007	0.013	0.013	0.025
River Rd	1.971	0.049	0.043	0.009	0.02	0.010	0.014
Surf City	0.421	0.078	0.072	0.007	0.014	0.014	0.024
Masonboro High Tide	0.42	0.044	Not flown	0.004	0.008	0.009	0.014
Masonboro Low Tide	0.047	0.047	0.080	0.004	0.008	0.009	0.014
Maysville	0.445	0.051	0.083	0.011	0.016	0.012	0.019
Carolina Bay	0.03	0.03	0.013	0.005	0.008	0.007	0.014

a low kappa coefficient, likely due to discrepancies with the NWI data initially used to generate GRPs for field data collection (see Fig. S2). When the model was applied to all sites combined using a large, consolidated training dataset, the overall accuracy reached 71.12%, with a kappa coefficient of 0.6443.

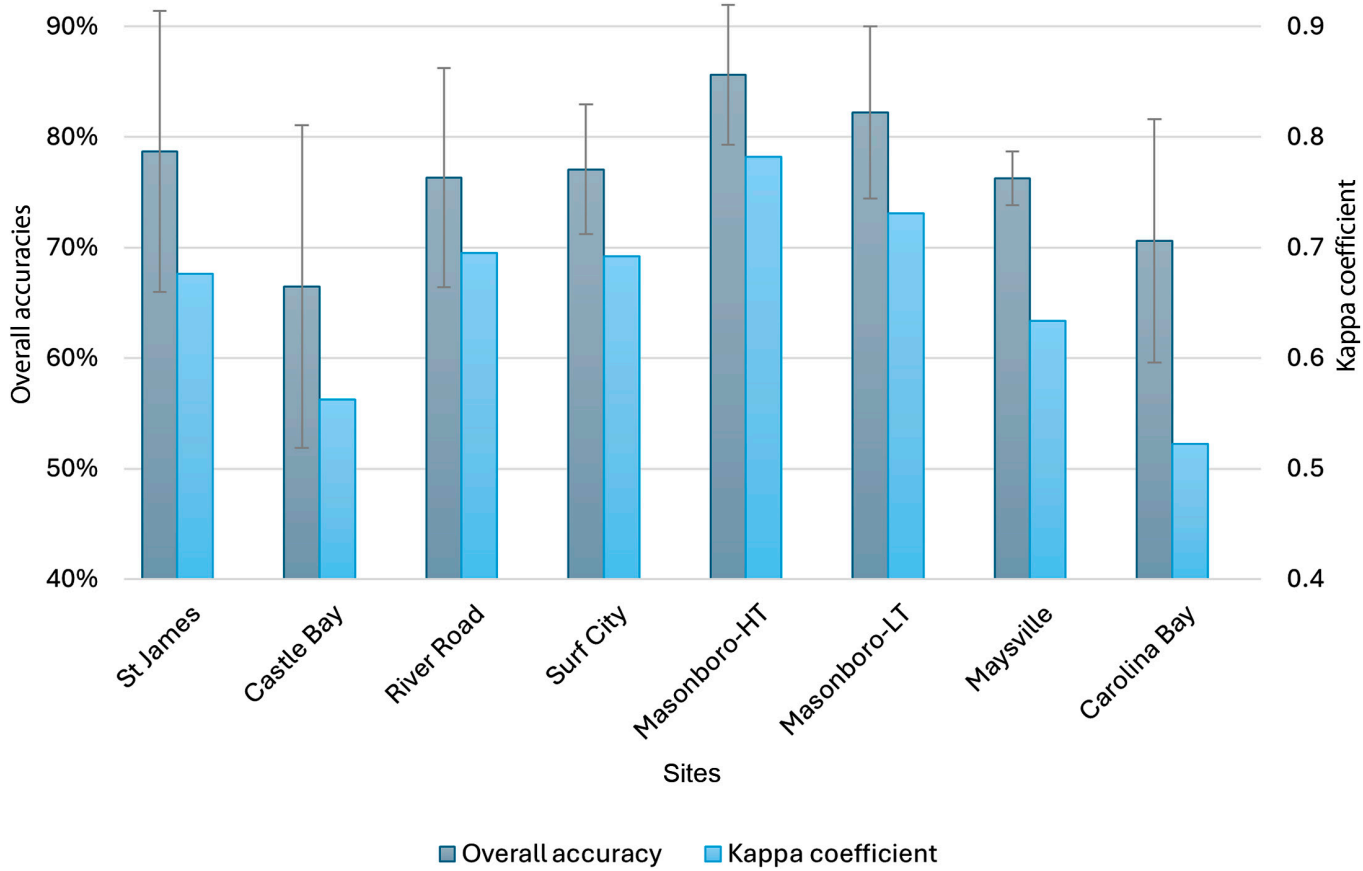

Fig. 4. Overall model classification accuracy and kappa coefficients for the 8 sites surveyed.

Although the accuracy metrics across the sites are not optimal, kappa values exceeding 0.61 are deemed to indicate substantial agreement and are considered acceptable [49]. To further evaluate the accuracy of our model, we conducted a spatial accuracy assessment to determine the distribution of correctly assigned GRPs to the final functional wetland classes, as classified by the RF model [42]. This assessment yielded an impressive 95% overall accuracy across the surveyed sites (Fig. S1A to C). We will delve into the accuracies specific to each functional wetland class in the subsequent section.

Classification accuracy by functional wetland type

The post-classification accuracy assessment results for each functional wetland type are presented in Table 3. For detailed classification results across all habitat classes, including nonwetland types, please refer to Table S1. The accuracy assessment is influenced by several factors: the predominant wetland type at the site, the relative distribution of each class within the site, and the number of GRPs in each class. Typically, classes that occupy smaller portions of the study areas, and thus have fewer GRPs, also exhibit lower accuracies.

In developing a land cover classification model, there is a critical juncture where the objective to achieve the most effective classification model for the project's goals surpasses the feasible number of accuracy assessment points available. Initially, we tested a binary wetland/nonwetland classification model, which, given satisfactory accuracy results against field-delineated and NWI assessments, was expanded to include multiple wetland classes in our final models. The presence of a single nonwetland class created confusion due to the spectrum of bare to upland forested areas at our sites. To address this, we categorized the habitat GRPs into 2 classes—"nonwetland open" and "nonwetland vegetated"—if they were located in areas predominantly featuring bare ground. Although this reclassification significantly reduced the number of nonwetland GRPs for these 2 categories, it stabilized the performance of the classification model (Table 5).

Moreover, the complexity of vertical vegetation at each site markedly influenced the overall model classification results. Sites dominated by forested palustrine vegetation demonstrated the lowest classification accuracy, followed by scrub–shrub and emergent types. This finding aligns with previous research indicating that mapping and classifying forested wetlands—including mangroves, which have received the bulk of attention, with less focus on palustrine forested wetlands—poses additional challenges in determining community composition and achieving high mapping accuracies [15–55].

The class-specific sensitivities and specificities for each site were generally higher than the overall model accuracy averaged across the 5 folds of the CV. However, certain wetland classes at some sites consistently exhibited low sensitivities. We hypothesize that these low sensitivities resulted from the limited extent of the training and testing areas. For instance, the area designated as palustrine scrub/shrub constituted only 0.58% of the total area covered across our study sites, suggesting that small areas with high vegetation complexity are more challenging to classify accurately compared to larger areas, even when vegetation complexity and within-class heterogeneity remain constant [40].

Table 5. Wetland class sensitivity, specificity, and user's and producer's accuracy for the 7 sites surveyed (8 total surveys)

Site name	Wetland class	Sensitivity	Specificity	User's accuracy	Producer's accuracy	Area (%)
St James	Palustrine forested	73.81%	84.85%	75.61%	73.81%	30.63%
	Palustrine scrub/shrub	78.95%	87.14%	76.92%	78.95%	49.20%
Castle Bay	Palustrine forested	78.26%	86.09%	69.23%	78.26%	40.04%
	Palustrine scrub/shrub	80.00%	95.21%	63.16%	80.00%	5.58%
	Palustrine emergent	0.00%	100.00%	0.00%	0.00%	0.05%
River Road	Palustrine forested	62.50%	85.26%	64.10%	62.50%	27.68%
	Palustrine emergent	85.29%	91.09%	76.32%	85.29%	45.53%
Surf City	Palustrine forested	85.29%	88.24%	67.44%	76.32%	33.22%
	Estuarine intertidal emergent	80.00%	92.13%	73.68%	93.33%	29.05%
	Palustrine scrub/shrub	84.00%	97.92%	62.50%	38.46%	1.46%
Masonboro-High Tide	Estuarine intertidal emergent	82.93%	94.64%	85.00%	82.93%	41.07%
Masonboro-Low Tide	Estuarine intertidal emergent	82.93%	92.79%	80.95%	82.93%	39.72%
Maysville	Palustrine forested	80.00%	80.00%	64.52%	80.00%	36.71%
Carolina Bay	Palustrine forested	89.29%	89.29%	25.00%	16.67%	9.91%
	Average palustrine forested ($N = 7$)	78.19%	85.62%	60.98%	64.59%	29.70%
	Average palustrine scrub/shrub ($N = 3$)	80.98%	93.42%	67.53%	65.80%	18.75%
	Average estuarine intertidal emergent ($N = 3$)	81.95%	93.19%	79.88%	86.40%	36.61%

The quality and detail of the final prediction maps are influenced by the spatial resolution of the data, the response variables, and the selected predictors. When juxtaposed with the most recent NWI data, our prediction maps displayed much more distinct and highly resolved wetland classes because of the hyperspatial resolution of the UAS data employed (Fig. 5).

In terms of classification accuracy for functional wetland classes, the estuarine intertidal emergent (E2EM) outperformed both palustrine forest (PFO) and palustrine scrub/shrub (PSS). E2EM achieved an average sensitivity of 81.95% and specificity of 93.19%, compared to 78.19% sensitivity and 85.62% specificity for PFO, and 80.98% sensitivity and 93.42% specificity for PSS. These metrics for all 3 classes are significantly better than the overall classification accuracy.

The higher accuracy for E2EM is attributed to the absence of complex forest structures, which often hinder the model's ability to distinguish between upland and wetland forests (Fig. 6). This challenge is evident at sites like River Road, Maysville, and Carolina Bay, where Palustrine Forest is the predominant wetland type and is interspersed with upland forested areas (Fig. 7).

Palustrine Scrub/Shrub mapping also presents difficulties due to its composition of shorter, woody plants, which can easily be confused with emergent wetlands and upland shrubs and grasslands. Despite these challenges, sites with extensive areas of PSS, such as St. James, Castle Bay, and River Road, displayed the highest accuracies for this class, albeit these are generally low at the class level [39] (Fig. 7).

Across the surveyed sites, the 3 wetland types—E2EM, PFO, and PSS—achieved class accuracies at or above the overall map accuracies. This indicates that the UAS LiDAR and multispectral imagery, combined with the RF classification method, yielded satisfactory results for wetland mapping, even with a reduced number of GRPs overall at the class level (Table S1).

Variable importance metrics for functional wetland type mapping and classification

The second research objective was to identify the most crucial variables (and the minimum number of predictor variables) that contribute to the classification of Coastal Plain wetlands and reflect the characteristics of the surveyed areas. Variable importance plots, which show the ranking of variables based on the mean decrease in model accuracy, were used for this analysis (see Fig. S3). In Table 6, to facilitate comparison across all sites, we adopted the ranking of each variable rather than the score itself, allowing us to assess the consistency in the importance of each variable across different locations. Variables with lower rankings (e.g., 1 or 2) were deemed more important than those with higher rankings (e.g., 10, 11, and 12). Additionally, the column "Count above 0.7" illustrates how often variable scores exceeded 0.7, indicating that a high score does not always correspond to the highest ranking due to the potential presence of multiple high-scoring variables in a model. For instance, Castle Bay had only 2 variables, DSM and canopy height, scoring above 0.7, whereas Masonboro LT had 6.

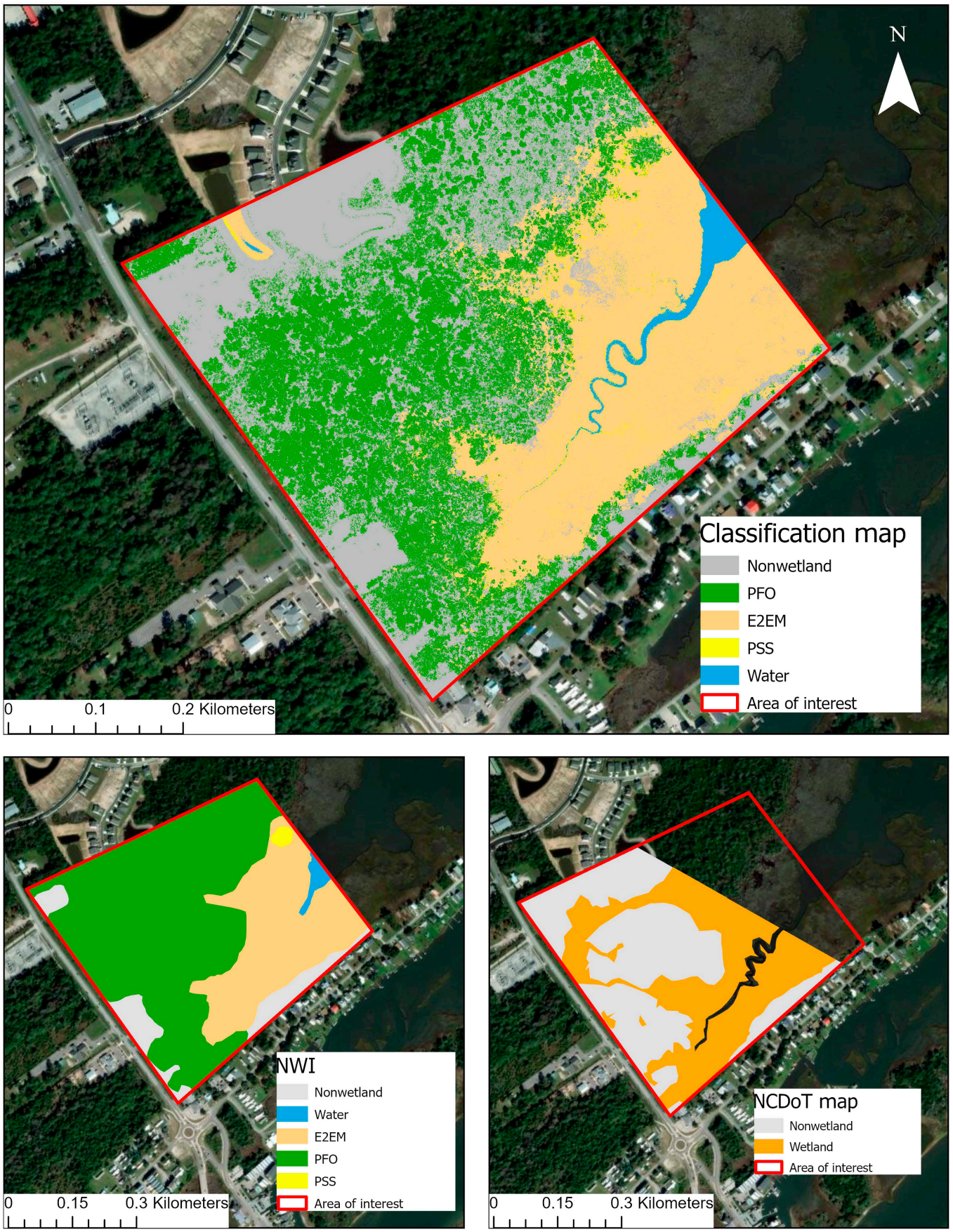

Fig. 5. Example model prediction (top panel) for the Surf City study site showing detailed wetland classes (palustrine forested, estuarine intertidal emergent, and palustrine scrub/shrub) compared with the NWI classification (bottom left) and the NC DOT wetland delineation (bottom right) created using traditional field methods.

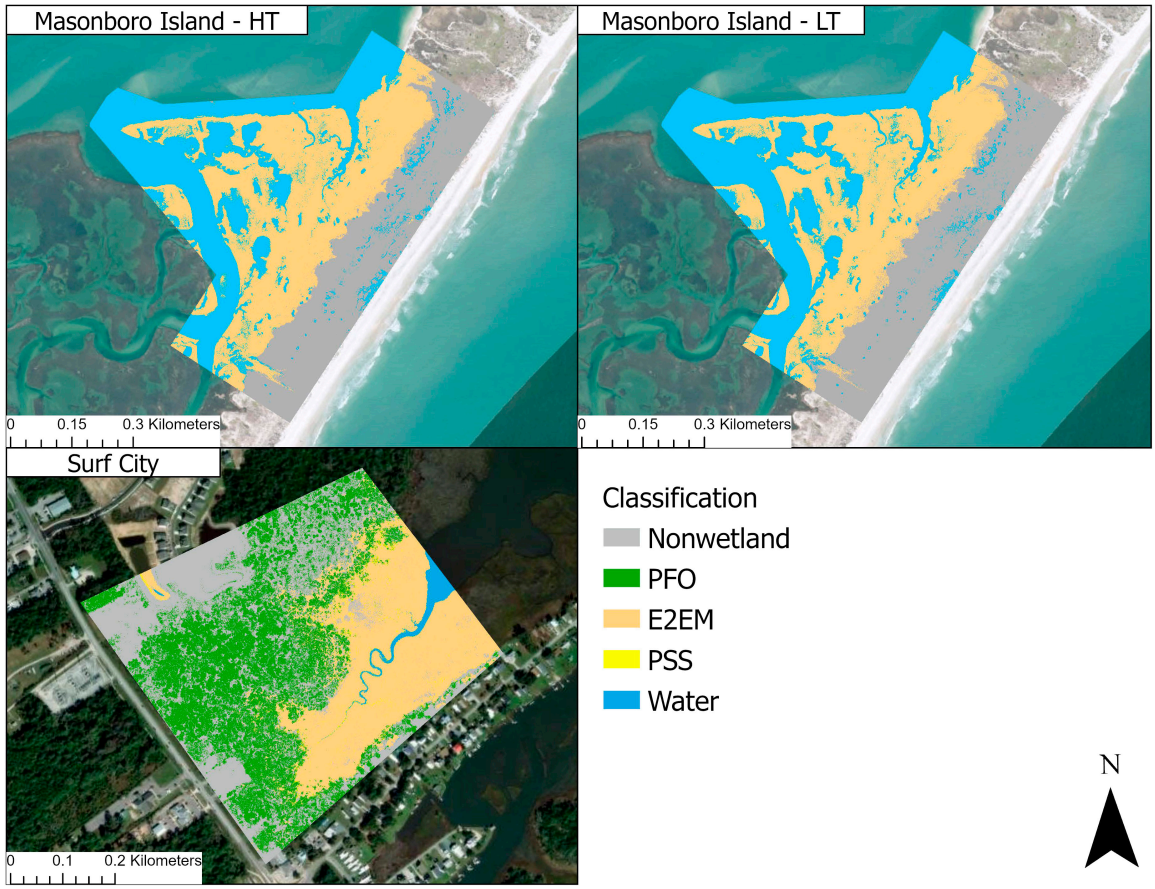

Fig. 6. Estuarine intertidal emergent wetland type dominated classifications for Masonboro high and low tide and Surf City study sites.

Using this ranking system, elevation variables derived from UAS LiDAR—such as DSM, DEM, smooth DEM, and hydro-condition DEM—along with canopy height and vegetation indices (NDVI, NDRE, and NDWI) from multispectral imagery, consistently ranked within the top 5 across all sites (Table 6). The inclusion of multispectral imagery significantly enhanced the performance of the RF models, with NDVI and NDWI frequently emerging as the top variables at most sites (6 and 5 instances, respectively, out of 9 classification models). Conversely, hydrological variables like flow direction and flow accumulation were among the least important, leading to their exclusion in the final model runs. The 3 curvature variables and aspect were generally not useful, with the exception of curvature at Castle Bay, which ranked fourth but scored below 0.7 (0.64).

These findings align with the general characteristics of the Coastal Plain area—predominantly flat landscapes covered by hydrophilic vegetation. Interestingly, canopy height exhibited significant variability in its importance, scoring above 0.7 at 3 sites but ranking as the least important (rank = 13) at 3 others, including Masonboro Island, which is dominated by low vegetation (emergent and scattered patches of upland grass and scrub/shrub). Although canopy height was not a top variable at sites dominated by salt marshes and low emergent vegetation, its role in assessing vegetation heights or microtopography as proxies for above-ground biomass or sediment accumulation rates in marshes is critically important and remains an area for further research [20,56]. At sites like Maysville and Castle Bay, where forest cover is complex and includes a mix of forested wetland and upland forest, canopy height data from LiDAR proved crucial, echoing findings by Zhang [57], Richardson et al. [58], and Albarnaz et al. [59]. When combined with both optical RGB and multispectral imagery, canopy height models (CHMs) significantly improve classification accuracies, regardless of the modeling framework employed [60]. Moreover, other LiDAR-derived variables like DSM and smoothed DEMs were also important, closely followed by DEMs and hydro-conditioned DEMs across the palustrine to estuarine gradient we surveyed.

Challenges, limitations, and future directions in functional wetland type mapping and classification

As noted by Guo et al. [30] in their comprehensive review of over 5,000 papers on wetland remote sensing, various techniques, datasets, and approaches have been employed for over 50 years to map, delineate, and classify wetlands, with a particular focus on coastal wetlands. They identified 2 main frontiers: the integration of multiple data sources, particularly optical and LiDAR data, to enhance classification accuracies, and the development of data collection methodologies, especially those that improve spatial and spectral resolution. Our study advances both frontiers by developing a methodology that combines UAS-collected and field reference data, integrating optical and multispectral collections with concurrent high-accuracy LiDAR surveys to derive functional wetland classifications across a range of wetland types.

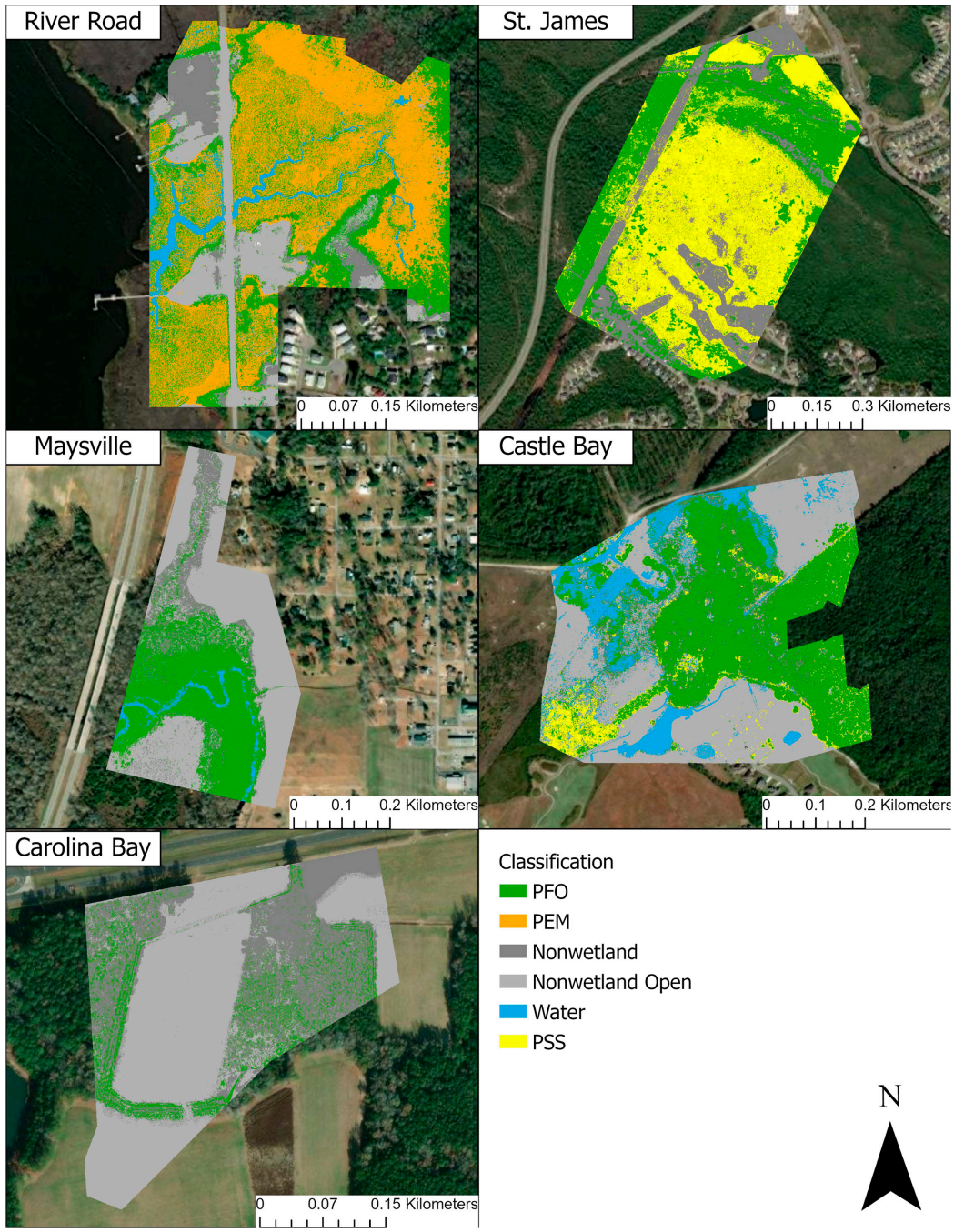

Fig. 7. Palustrine forested and palustrine scrub–shrub wetland type dominated classifications for River Road, St. James, Castle Bay, Maysville, and Carolina Bay study sites.

One limitation of this research was the difficulty in accessing most of the sampled areas and the challenge of supplementing our field-collected training data with high-quality response variable data, hindered by the outdated NWI wetland extent data for North Carolina. Accurate and up-to-date GRPs are crucial for creating high-quality and precise wetland classifications [25]. Additionally, limited accessibility due to water and mud cover and the challenge of distinguishing between forested and scrub–shrub classes during visual inspections using NAIP or even high-resolution multispectral UAS imagery complicated the creation of additional training and validation data. However, focusing solely on accuracy metrics for our classification at the functional class level for 3 major classes of interest—palustrine forested, shrub, and estuarine emergent—and accepting a margin of error (MOE) estimate of 7 to 10%, allowed us to utilize relatively small sample sizes for model training and validation [39,61].

If the ultimate goal is to enhance the accuracy of Coastal Plain wetland prediction models, improving the quality of response data remains a high priority for any future mapping and modeling project using UAS technology. Future approaches could involve using polygon sample data, rather than point data, to cover a larger area [62,63]. Additionally, models parameterized with different predictor variables than

Table 6. Variable scores (ranging from 0.0 to 1.0) were converted to ranks (ordered from 1 to 13) indicating the strength, or importance, of each variable. Variables with scores above 0.7 are in bold font, indicating how many and which variables at each study site are important to derive the classification.

Variable name	St James	Castle Bay	River Rd	Surf City	Masonboro HT	Masonboro LT	Maysville	Carolina Bay	Count above 0.7
DSM	8	**1**	7	**2**	6	**6**	5	**1**	4
DEM	5	5	5	**4**	5	**5**	3	9	2
Smooth DEM	**2**	6	4	7	**3**	**1**	2	8	3
Hydro-DEM	7	3	3	**1**	4	**2**	4	12	2
Canopy Height	6	**2**	13	**5**	13	13	**1**	3	3
Aspect	9	13	8	11	8	11	10	11	0
Slope	4	7	11	9	9	9	7	**2**	1
Curvature	13	12	10	13	10	8	13	4	0
Plan Curvature	10	9	9	12	11	12	8	7	0
Profile Curvature	12	11	12	10	12	10	11	10	0
NDVI	**1**	8	**2**	**3**	**1**	**3**	6	6	5
NDWI	**3**	4	**1**	6	**2**	**4**	12	5	4
NDRE	11	10	6	8	7	7	9	13	0

those chosen for this research should be considered to refine the moderately good results, partially influenced by our selection of predictor variables in line with current wetland mapping programs in North Carolina [64]. Future iterations of this work will also explore object-based image analysis (OBIA) approaches, which tend to perform better than pixel-based methods when utilizing high-resolution drone imagery [65]. Moreover, different machine learning classifications, such as various ensemble methods like gradient boosting [61,66,67] and deep learning classification methods [60], will be tested to compare model performance. However, these advanced machine learning modeling approaches typically require a much larger amount of training data, which could be obtained through field collection, on-screen digitization, or a combination of both.

Conclusion

In conclusion, this study has demonstrated the powerful capabilities of unmanned aerial systems (UASs) for the collection of LiDAR and multispectral imagery, significantly enhancing the classification and mapping of various wetland types across the coastal plain. A key innovation was achieving an optimized balance between flight altitude and line overlap for UAS LiDAR collections—specifically a flight altitude of 60 m with a 25% overlap—proving to be most effective across the surveyed sites. The high-quality LiDAR data obtained from these optimized flight parameters played a pivotal role in accurately classifying functional wetland types through the integration of elevation data and vertical vegetation metrics from UAS LiDAR datasets with multispectral-derived indices.

Furthermore, the study highlighted the critical ecological role of coastal wetlands as natural buffers against floods and storm surges, emphasizing the urgent need for updated maps and spatial models to effectively assess and maintain their ecosystem services. By utilizing models parameterized with UAS-collected LiDAR and multispectral data and trained using habitat GRPs and on-the-ground wetland delineations, the research achieved moderately spatially accurate wetland delineations compared to National Wetlands Inventory (NWI) data.

The research also underscored the importance of highly resolved topographic variables such as DSMs and smoothed and hydro-conditioned DEMs, alongside vegetation height and indices (NDVI and NDWI), as crucial predictors for wetland presence. This integrative approach using UAS technology for wetland mapping and classification presents a replicable study design that substantially advances the field of coastal wetland mapping. It further exemplifies the successful integration of optical multispectral imagery with active remote sensing techniques, bolstering efforts in wetland prediction and classification.

The study's results not only showcase the potential of UAS technology but also point to the necessity of collecting more habitat points to improve overall accuracies and class-specific sensitivities for specific mapping projects. The challenges encountered, particularly those related to accessibility and the limitations of the current methodologies, underscore the ongoing need for methodological advancements in the remote sensing of wetland environments. These results suggest potential areas for further development, such as the use of OBIA and advanced machine learning techniques like deep learning, to enhance classification accuracy and efficiency in future wetland mapping and monitoring endeavors.

Overall, this research provides valuable insights and lays a robust foundation for future studies aiming to refine the accuracy, efficiency, and functionality of wetland mapping and monitoring using advanced remote sensing technologies. It stresses the importance of continuous improvement in data collection strategies and the integration of diverse remote sensing data types to effectively capture the dynamic nature of wetland ecosystems.

Acknowledgments

We would like to thank the NCDOT for facilitating and funding this research and extend a special thanks to M. Weatherford for his continued support of this project. We would also like to extend a special thanks to Y. Marsan, laboratories manager in the Department of Earth and Ocean Sciences, for providing unconditional support during field surveys and research associate K. Mapes and former UNCW Earth and Ocean Sciences Department graduate students J. Scopa, C. Eckhardt, J. Giddens, and B. Baxley for assistance during data collection for this project.

Funding: This research was funded by the North Carolina Department of Transportation (NCDOT), contract number RP 2020–04, awarded to N.G.P. (lead principal investigator) and J.N.H. in the Department of Earth and Ocean Sciences at the University of North Carolina Wilmington. The funders had no role in the design of the study; in the collection, analyses, or interpretation of data; in the writing of the manuscript; or in the decision to publish the results.

Author contributions: Conceptualization: N.G.P. Methodology: N.G.P., A.M., and J.N.H. Software: N.G.P. and A.M. Validation: A.M. and N.G.P. Formal analysis: A.M., N.G.P., C.C., and Y.W. Investigation: N.G.P. and J.N.H. Resources: N.G.P. Data curation: A.M., N.G.P., C.C., and Y.W. Writing—original draft preparation: N.G.P. and E.G.D. Writing—review and editing: N.G.P. and J.N.H. Visualization: A.M. and E.G.D. Supervision: N.G.P. Project administration: N.G.P. Funding acquisition: N.G.P. and J.N.H. All authors have read and agreed to the published version of the manuscript.

Competing interests: The authors declare that they have no competing interests.

Data Availability

Data and codes used in this project can be made available upon request from both the researchers and the NCDOT.

Supplementary Materials

Figs. S1 to S3
Table S1

References

1. Dillabaugh KA, King DJ. Riparian marshland composition and biomass mapping using Ikonos imagery. *Can J Remote Sens*. 2008;34(2):143–158.
2. Walker W. 2010 Wetland mapping summary. 2011. [retrieved 20 Sept 2021].
3. Durgan SD, Zhang C, Ducaster A, Fourney F, Su H. Unmanned aircraft system photogrammetry for mapping diverse vegetation species in a heterogeneous coastal wetland. *Wetlands*. 2020;40:2621–2633.
4. Klemas V. Remote sensing of coastal wetland biomass: An overview. *J Coast Res*. 2013b;290(5):1016–1028.
5. Campbell C, Vitt DH, Halsey LA, Campbell ID, Thormann MN, Bayley SE. *Net primary production and standing biomass in northern continental wetlands. Information Report NOR-X369*. Edmonton, Alberta: Natural Resources Canada; 2000.
6. Luo S, Wang C, Pan F, Xi X, Li G, Nie S, Xia S. Estimation of wetland vegetation height and leaf area index using airborne laser scanning data. *Ecol Indic*. 2015;48:550–559.
7. Kirwan ML, Megonigal JP. Tidal wetland stability in the face of human impacts and sea-level rise. *Nature*. 2013;504(7478):53–60.
8. Kalacska M, Chmura GL, Lucanus O, Bérubé D, Arroyo-Mora JP. Structure from motion will revolutionize analyses of tidal wetland landscapes. *Remote Sens Environ*. 2017;199:14–24.
9. Pricope NG, Halls JN, Mapes KL, Baxley JB, Wu JJ. Quantitative comparison of UAS-borne LiDAR systems for high-resolution forested wetland mapping. *Sensors*. 2020;20(16):4453.
10. Jeziorska J. UAS for wetland mapping and hydrological modeling. *Remote Sens*. 2019;11(17):1997.
11. Gale S. *National wetlands inventory (NWI) accuracy in North Carolina*. Falls Church (VA): U.S. Fish and Wildlife Service; 2021.
12. Kim J, Popescu SC, Lopez RR, Wu XB, Silvy NJ. Vegetation mapping of No Name Key, Florida using lidar and multispectral remote sensing. *Int J Remote Sens*. 2020;41(24):9469–9506.
13. Greenberg JA, Dobrowski SZ, Ustin SL. Shadow allometry: Estimating tree structural parameters using hyperspatial image analysis. *Remote Sens Environ*. 2005;97(1):15–25.
14. De Boisvilliers M, Selve M. UAS Lidar for ecological restoration of wetlands. *GIM Int*. 2019;33(2):29–31.
15. Hogg AR, Todd KW. Automated discrimination of upland and wetland using terrain derivatives. *Can J Remote Sens*. 2007;33(Sup 1):S68–S83.
16. Lefsky MA, Cohen WB, Parker GG, Harding DJ. Lidar remote sensing for ecosystem studies. *Bioscience*. 2002;52(1):19–30.
17. Millard K, Richardson M. Wetland mapping with LiDAR derivatives, SAR polarimetric decompositions, and LiDAR-SAR fusion using a random forest classifier. *Can J Remote Sens*. 2013;39(4):290–307.
18. Pricope NG, Minei A, Halls JN, Chen C, Wang Y. UAS hyperspatial LiDAR data performance in delineation and classification across a gradient of wetland types. *Drones*. 2022;6(10):268.
19. Ritchie JC. Remote sensing applications to hydrology: Airborne laser altimeters. *Hydrol Sci J*. 1996;41(4):625–636.
20. DiGiacomo AE, Bird CN, Pan VG, Dobroski K, Atkins-Davis C, Johnston DW, Ridge JT. Modeling salt marsh vegetation height using unoccupied aircraft systems and structure from motion. *Remote Sens*. 2020;12(14):2333.
21. Rotnicka J, Dłużewski M, Dąbski M, Rodzewicz M, Włodarski W, Zmarz A. Accuracy of the UAV-based DEM of beach–foredune topography in relation to selected morphometric variables, land cover, and multitemporal sediment budget. *Estuar Coasts*. 2020;43:1939–1955.
22. Chust G, Galparsoro I, Borja Á, Franco J, Uriarte A. Coastal and estuarine habitat mapping, using LiDAR height and intensity and multi-spectral imagery. *Estuar Coast Shelf Sci*. 2008;78(4):633–643.
23. Rapinel S, Hubert-Moy L, Clement B. Combined use of LiDAR data and multispectral earth observation imagery for wetland habitat mapping. *Int J Appl Earth Obs Geoinf*. 2015;37:56–64.

24. Mohri M, Rostamizadeh A, Talwalkar A. *Foundations of machine learning*. Cambridge (MA): MIT Press; 2018.
25. O'Neil GL, Goodall JL, Watson LT. Evaluating the potential for site-specific modification of LiDAR DEM derivatives to improve environmental planning-scale wetland identification using random forest classification. *J Hydrol*. 2018;559:192–208.
26. Tian SH, Zhang XF, Tian J, Sun Q. Random forest classification of wetland landcovers from multi-sensor data in the arid region of Xinjiang China. *Remote Sens*. 2016;8(11):954.
27. Breiman L. Random forests. *Mach Learn*. 2001;45(1):5–32.
28. Martinez-Taboada F, Redondo JI. Variable importance plot (mean decrease accuracy and mean decrease Gini). *PLOS ONE*. 2020;**15**(4):e0230799.
29. Wei PF, Lu ZZ, Song JW. Variable importance analysis: A comprehensive review. *Reliab Eng Syst Saf*. 2015;142:399–432.
30. Guo M, Li J, Sheng C, Xu J, Wu L. A review of wetland remote sensing. *Sensors*. 2017;17(4):777.
31. LePage B. *Wetlands: Integrating multidisciplinary concepts*. Dordrecht (Netherlands): Springer; 2011. p. 1–261.
32. Committee FGD. *Classification of wetlands and deepwater habitats of the United States*. 2nd ed. Washington (DC): U.S. Fish and Wildlife Service; 2013.
33. Berra EF, Peppa MV. Advances and challenges of UAV SFM MVS photogrammetry and remote sensing: Short review. Paper presented at: 2020 IEEE Latin American GRSS & ISPRS Remote Sensing Conference (LAGIRS); 2020; Hannover, Germany.
34. Kholil M, Ismanto I, Fu'ad MN. 3D reconstruction using structure from motion (SFM) algorithm and multi-view stereo (MVS) based on computer vision. *IOP Conf Ser Mater Sci Eng*. 2021;1073(1):Article 012066.
35. Smith MW, Carrivick JL, Quincey DJ. Structure from motion photogrammetry in physical geography. *Prog Phys Geogr*. 2016;40(2):247–275.
36. Aiello S, Eckstrand E, Fu A, Landry M, Aboyoun P. Machine learning with R and H2O. 2018. [accessed 6 May 2022] http://h2o.ai/resources/.
37. R Core Team. R: A language and environment for statistical computing. R Foundation for Statistical Computing. 2020. [accessed 6 May 2022] https://www.r-project.org/
38. Berrar D. Cross-validation. In: *Encyclopedia of bioinformatics and computational biology*. Hannover (Germany): International Society for Photogrammetry and Remote Sensing (ISPRS); 2019. p. 542–545.
39. Foody GM, Mathur A, Sanchez-Hernandez C, Boyd DS. Training set size requirements for the classification of a specific class. *Remote Sens Environ*. 2006;104(1):1–14.
40. Ramezan C, Warner T, Maxwell A, Price B. Effects of training set size on supervised machine-learning land-cover classification of large-area high-resolution remotely sensed data. *Remote Sens*. 2021;13(3):368.
41. Rodriguez-Martinez C, Torres-Sospedra J. Revisiting the analysis of hyperparameters in k-NN for Wi-Fi and BLE fingerprinting: Current status and general results. Paper presented at: 2021 International Conference on Indoor Positioning and Indoor Navigation (IPIN); 29 Nov–2 Dec 2021; Lloret de Mar, Spain.
42. Comber A, Fisher P, Brunsdon C, Khmag A. Spatial analysis of remote sensing image classification accuracy. *Remote Sens Environ*. 2012;127:237–246.
43. Mesas-Carrascosa F-J, Notario García M, Meroño de Larriva JE, García-Ferrer A. An analysis of the influence of flight parameters in the generation of unmanned aerial vehicle (UAV) orthomosaicks to survey archaeological areas. *Sensors*. 2016;16(11):1838.
44. Sofonia JJ, Phinn S, Roelfsema C, Kendoul F, Rist Y. Modelling the effects of fundamental UAV flight parameters on lidar point clouds to facilitate objectives-based planning. *ISPRS J Photogramm Remote Sens*. 2019;149:105–118.
45. Alsadik B, Remondino F. Flight planning for LIDAR-based UAS mapping applications. *ISPRS Int J Geo Inf*. 2020;9(6):378.
46. Chadwick J. Integrated LiDAR and IKONOS multispectral imagery for mapping mangrove distribution and physical properties. *Int J Remote Sens*. 2011;32(21):6765–6781.
47. Huang C, Peng Y, Lang M, Yeo IY, McCarty G. Wetland inundation mapping and change monitoring using Landsat and airborne LiDAR data. *Remote Sens Environ*. 2014;141:231–242.
48. Pavri F, Dailey A, Valentine V. Integrating multispectral ASTER and LiDAR data to characterize coastal wetland landscapes in the northeastern United States. *Geocarto Int*. 2012;26(8):647–661.
49. McHugh ML. Interrater reliability: The kappa statistic. *Biochem Med*. 2012;22(3):276–282.
50. Conchedda G, Durieux L, Mayaux P. An object-based method for mapping and change analysis in mangrove ecosystems. *ISPRS J Photogramm Remote Sens*. 2008;63(5):578–589.
51. Gao J. A hybrid method toward accurate mapping of mangroves in a marginal habitat from SPOT multispectral data. *Int J Remote Sens*. 1998;19(10):1887–1899.
52. Heumann BW. An object-based classification of mangroves using a hybrid decision tree—Support vector machine approach. *Remote Sens*. 2011;3(11):2440–2460.
53. Huang X, Zhang L, Wang L. Evaluation of morphological texture features for mangrove forest mapping and species discrimination using multispectral IKONOS imagery. *IEEE Geosci Remote Sens Lett*. 2009;6(3):393–397.
54. Vogt J, Kautz M, Herazo MLF, Triet T, Walther D, Saint-Paul U, Diele K, Berger U. Do canopy disturbances drive forest plantations into more natural conditions? A case study from Can Gio Biosphere Reserve, Viet Nam. *Glob Planet Chang*. 2013;110(Part B):249–258.
55. Wang Y. Seasonal change in the extent of inundation on floodplains detected by JERS-1 Synthetic Aperture Radar data. *Int J Remote Sens*. 2004;25(13):2497–2508.
56. Ensign S, Noe G. Tidal extension and sea level rise: Recommendations for a research agenda. *Front Ecol Environ*. 2018;16(1):37–43.
57. Zhang K. Identification of gaps in mangrove forests with airborne LiDAR. *Remote Sens Environ*. 2008;112(5):2309–2325.
58. Richardson MC, Mitchell CPJ, Branfireun BA, Kolka RK. Analysis of airborne LiDAR surveys to quantify the characteristic morphologies of northern forested wetlands. *J Geophys Res Biogeosci*. 2010;115:G00H03.
59. Albarnaz JD, Toso J, Corrêa AA, Simes CMO, Barardi CRM. Assessment of airborne scanning laser altimetry (LIDAR) in a deltaic wetland environment. *Can J Remote Sens*. 2003;29(6):718–728.
60. Gonzalez-Perez A, Abd-Elrahman A, Wilkinson B, Johnson DJ, Carthy RR. Deep and machine learning image classification of coastal wetlands using unpiloted aircraft system multispectral images and LiDAR datasets. *Remote Sens*. 2022;14:3937.
61. Wen L, Hughes M. Coastal wetland mapping using ensemble learning algorithms: A comparative study of bagging, boosting, and stacking techniques. *Remote Sens*. 2020;12(10):1683.

62. Gaughan A, Kolarik N, Stevens F, Pricope NG, Cassidy L, Salerno J, Bailey K, Drake M, Woodward K, Hartter J. Using very high-resolution multispectral classification to estimate savanna fractional vegetation coverage. *Remote Sens*. 2022;14(3):551.
63. Kolarik N, Gaughan A, Stevens F, Pricope NG, Woodward K, Cassidy L, Salerno J, Hartter J. A multi-plot assessment of vegetation structure using a micro-unmanned aerial system (UAS) in a semi-arid savanna environment. *ISPRS J Photogramm Remote Sens*. 2020;164:84–96.
64. Wang S-G, Deng J, Chen M, Weatherford M, Paugh L. Random forest classification and automation for wetland identification based on DEM derivatives. Paper presented at: *Proceedings of the 2015 International Conference on Ecology and Transportation (ICOET)*; 2015.
65. Ventura D, Napoleone F, Cannucci S, Alleaume S, Valentini E, Casoli E, Burrascano S. Integrating low-altitude drone-based imagery and OBIA for mapping and managing semi-natural grassland habitats. *J Environ Manag*. 2022;321:Article 115723.
66. Govil S, Lee AJ, MacQueen AC, Pricope NG, Minei A, Chen C. Using hyperspatial LiDAR and multispectral imaging to identify coastal wetlands using gradient boosting methods. *Remote Sens*. 2022;14(23):6002.
67. Sun S, Zhang Y, Song Z, Chen B, Zhang Y, Yuan W, Chen C, Chen W, Ran X, Wang Y. Mapping coastal wetlands of the Bohai rim at a spatial resolution of 10 m using multiple open-access satellite data and terrain indices. *Remote Sens*. 2020;12:4114.
68. Li Z, Zhu C, Gold C. *Digital terrain modeling: Principles and methodology*. 1st ed. Boca Raton (FL): CRC Press; 2005.
69. Vieux BE. DEM aggregation and smoothing effects on surface runoff modeling. *J Comput Civ Eng*. 1993;7(3):310–338.
70. Maathuis BHP, Msc L. Digital elevation model based hydro-processing. *Geocarto Int*. 2006;21(1):21–26.
71. Wilson DJ, Gallant JC. Digital terrain analysis. In: Wilson DJ, Gallant JC, editors. *Terrain analysis: Principles and applications*. Hoboken (NJ): John Wiley & Sons; 2000. p. 1 –27.
72. Tucker CJ. Red and photographic infrared linear combinations for monitoring vegetation. *Remote Sens Environ*. 1979;8(2): 127–150.
73. Gao B-C. NDWI—A normalized difference water index for remote sensing of vegetation liquid water from space. *Remote Sens Environ*. 1996;58(3):257–266.
74. Barnes EM, Clarke TR, Richards SE, Colaizzi PD, Haberland J, Kostrzewski M, Lascano RJ. Coincident detection of crop water stress, nitrogen status and canopy density using ground based multispectral data. Paper presented at: Proceedings of the Fifth International Conference on Precision Agriculture; 2000; Bloomington, MN, USA.
75. Lefsky MA. *Application of lidar remote sensing to the estimation of forest canopy and stand structure*. Charlottesville (VA): University of Virginia; 1997.